Study of alternatives and experimental validation for predictions of hole-edge fatigue crack growth in 42CrMo4 steel

Mikel Escalero[a,b,*], Sergio Blasón[b], Haritz Zabala[a], Ireneo Torca[c], Iker Urresti[a], Miguel Muniz-Calvente[b], Alfonso Fernández-Canteli[b]

[a] *Structural Reliability Department, Mechanics Area, IK4-Ikerlan Technology Research Center. P J.M. Arizmendiarreta Ibilbidea, 2, 20500 Arrasate-Mondragón, Spain.*
[b] *Department of Construction and Manufacturing Engineering, University of Oviedo. C\|Pedro Puig Adam, s/n, 33204 Gijón, Spain.*
[c] *Mechanical and Manufacturing Department, Engineering Faculty of Mondragon University. Loramendi, 4, 20500 Arrasate-Mondragon, Spain.*

Abstract

The objective of this work is to establish pertinent criteria allowing an optimal alternative to be chosen for calculating the inputs needed to make Run/Repair/Replace decisions and to program inspection plans for cracked wind turbine bearing rings. With this aim, the growth of a hole-edge through-crack was predicted analytically, simulated and measured in a 42CrMo4 steel plate subjected to mode-I cyclic loading. Different alternative procedures according to BS 7910:2013 fitness-for-service code were implemented. Unexpectedly, the numerical calculation of the local stresses in the uncracked body did not improve the estimations of the critical crack length and the number of cycles to failure performed following purely analytical alternatives. That alternative underestimated the critical crack length by 50%. Among the alternatives studied, the one based on numerically calibrated stress intensity factors and crack growth coefficients characterized at the corresponding stress ratios proved to be the most suitable one. Following that alternative, the fatigue life was found to be overestimated by 3.96% in the best scenario whereas the critical crack length was underestimated with an error less than 3%, determined using the Failure Assessment Diagram (FAD) as a failure criterion.

Keywords: Fatigue crack growth, fitness-for-service, bearing ring, BS 7910:2013, alternative predictions, experimental validation.

*Corresponding author
Email address: mescalero@ikerlan.es (Mikel Escalero)

Nomenclature

Latin characters

a	Crack length (mm)
$\mathrm{d}a/\mathrm{d}N$	Crack growth rate (mm/cycle)
E	Young's modulus (GPa)
e	Thickness of the component (mm)
f	Crack opening function (-)
H	Width of the component (mm)
K	Stress intensity factor ($\mathrm{MPa\,mm^{1/2}}$)
L	Load (N)
M	Geometric factor (-)
N	Number of cycles (-)
P	Applied axial force (N)
R	Stress ratio (-)

Greek characters

ε	Strain (-)
σ	Strength, normal stress (MPa)

Subscripts and superscripts

$()_{\mathrm{b}}$	Bending
$()_{\mathrm{c}}$	Critical
$()_{\mathrm{m}}$	Membrane
$()^{\mathrm{loc}}$	Local
$()_{\mathrm{max}}$	Maximum
$()_{\mathrm{r}}$	Ratio
$()^{\mathrm{rem}}$	Remote
$()_{\mathrm{th}}$	Threshold
$()_{\mathrm{u}}$	Ultimate
$()_{\mathrm{y}}$	Yield

Abbreviations

CT	Compact Tension
FAD	Failure Assessment Diagram
FEA	Finite Element Analysis
SIF	Stress Intensity Factor

1. Introduction and motivation

Fatigue crack growth represents one of the predominant failure mechanisms in bearings used for pitch rotation of wind turbine blades (see Figure 1a). In particular, the in-service cracking of the outer ring is a major issue, as it has been reported by many bearing manufacturers from the wind energy industry [1]. This ring displays holes at a regular distance for bolt tightening, grease fittings and other handling and maintenance operations, which act as stress concentrators giving rise to local concentrations of the nominal stresses. At a given point along the lifetime of the bearing, a crack may initiate at the edge of a hole where stresses reach maximum values. Firstly, the crack propagates as a surface crack, afterwards evolving to a through-crack that leads eventually to a catastrophic failure of the ring, as shown in Figure 1b [1].

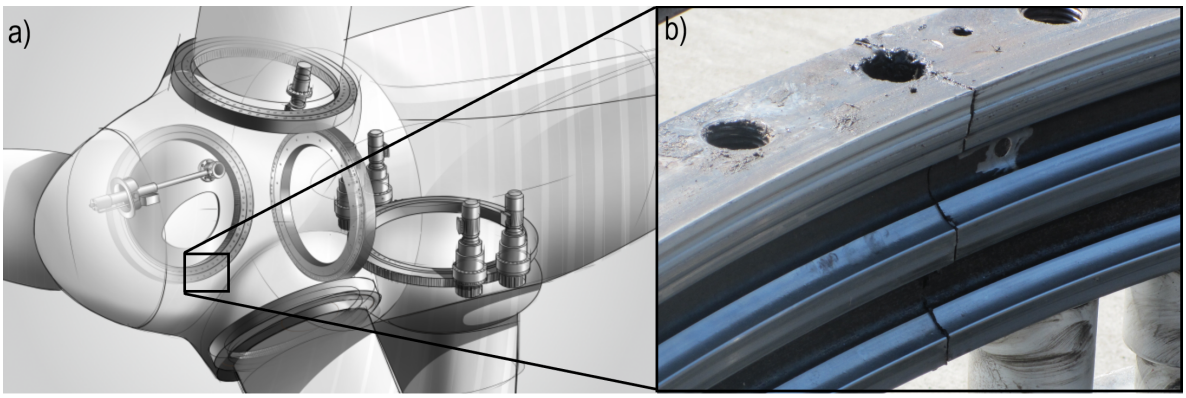

Figure 1: a) Schematic representation of a wind turbine and some internal components [2]. b) A real blade bearing ring broken during operation (courtesy of RBB Engineering © [1]).

Such components are usually made of 42CrMo4 steel, which exhibits excellent hardenability properties allowing high hardness to be achieved on the raceway [3]. Regarding loading conditions, the critical location where the crack initiates is subjected to multiaxial variable amplitude stresses, generated by the tightening preload of the bolts and the wind and inertial loads transmitted from the blades through the rolling elements. Nevertheless, the variable component of the total stress tensor causing fatigue cracking is predominantly uniaxial in the hoop direction, what explains the mode-I growth observed in Figure 1b [1].

In order to make Run/Repair/Replace decisions and to program inspection plans for cracked bearing rings, the following parameters must be considered: 1) critical crack length and 2) number of cycles to failure. These parameters can be calculated by a crack propagation analysis performed according to fitness-for-service procedures as those proposed in BS 7910:2013 [4–6]. In any case, lifetime predictions are performed by integrating crack growth law, taking the Stress Intensity Factor (SIF) range as an input, until the sudden failure is detected by evaluating the Failure Assessment Diagram (FAD) [7]. However, the BS 7910:2013 standard allows different alternatives for lifetime prediction to be applied, which differ in terms of prediction accuracy and invested assessment time. The computation of SIF ranges and FAD evaluation may be done analytically resorting to closed form formulas of different standardized geometries [7] or numerically, using Finite Element Analysis (FEA) [8–10]. For

computing the crack growth rate, a number of crack growth laws are available [11] either using crack growth coefficients taken from literature or characterized ad hoc.

Fatigue crack growth has drawn the attention of many researchers in the last decades [12–16] and has become a mature field of study. More specifically, extensive research has been conducted regarding crack growth near holes or circular notches [17–22]. However, a remarkable lack of comparative studies is noticed that quantify and justify discrepancies between the different predictions resulting for real cases based on aforementioned alternative procedures.

The objective of this work is to establish pertinent criteria allowing an optimal alternative to be chosen for calculating the inputs needed to make Run/Repair/Replace decisions and to program inspection plans for cracked wind turbine bearing rings. With this aim, the crack growth in the larger ligament of a drilled plate made of 42CrMo4 steel, subjected to mode-I cyclic loading (Figure 2) is studied. Crack propagation is predicted according to the alternatives mentioned above and is also simulated jointly using the FRANC3D and ANSYS codes. An experimental campaign is conducted, in which real components are tested under three different load ranges and stress ratios. Finally, the experimental lifetime data are compared with the simulated and analytically derived results, providing useful guidance for practical design of wind turbine bearing rings.

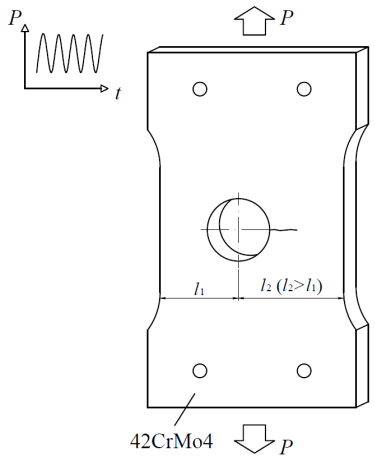

Figure 2: Structural detail studied in this work.

2. Crack growth predictions based on BS 7910:2013

The methodology proposed for predicting the evolution of a growing crack from the edge of a hole in a plate subjected to mode-I cyclic load (Figure 2) is depicted in Figure 3. This methodology complies with guidelines and recommendations given in BS 7910:2013 [7] (*Guide to methods for assessing the acceptability of flaws in metallic structures*).

The analyst has to introduce crack and body dimensions and the maximum and minimum values of the applied load as input. Additional material data are needed, namely, tensile properties, crack growth curve coefficients at the particular stress ratio, threshold stress intensity factor range and

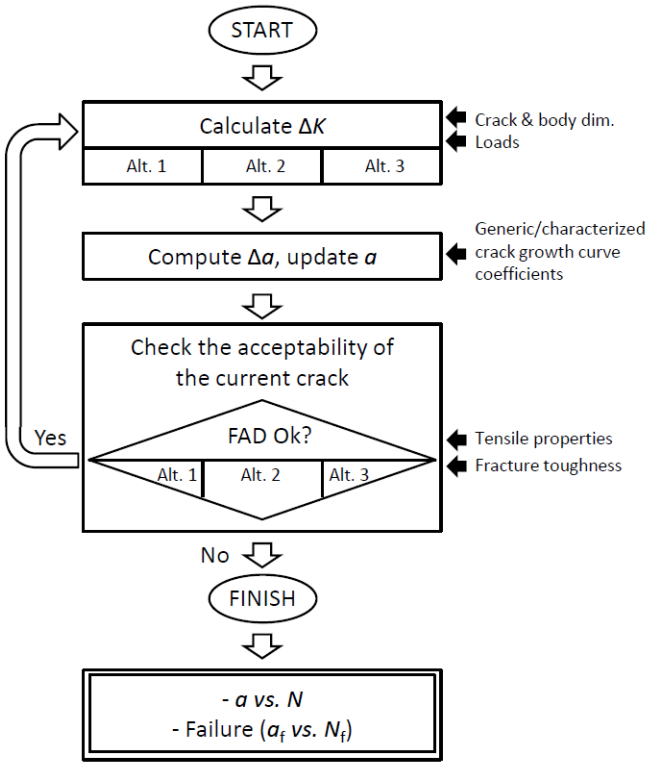

Figure 3: Methodology for predicting crack growth in the studied case.

fracture toughness. The main output is the crack length progress as a function of the number of cycles, from the initial crack until the catastrophic failure.

The algorithm is based on an iterative procedure consisting of three main steps: 1) calculation of the stress intensity factor range within one single cycle, 2) computation of the crack advance and updating of the crack length and 3) verification of crack acceptability according to the Failure Assessment Diagram (FAD). The computation procedure ends when unacceptable conditions are encountered.

In step 1), the variation of the stress intensity factor is calculated, which represents a valid fracture parameter under the hypothesis of linear elastic behavior of the 42CrMo4 steel. For this particular geometry, no closed-form formulas are available in the literature for calculating the SIF as a function of stresses or applied loads. Therefore, the SIF may be either approximated using expressions corresponding to similar predefined geometries or computed by finite element analysis of the actual flawed body. In either approach, analytical or numerical, the study case is simplified to a one-dimensional problem. A single value of SIF is computed for the entire crack front and all its points are considered to advance the same extent, restricting the front shape to be straight.

In step 2), the crack extension is computed and the crack dimension is updated. With this aim, crack growth rate is calculated substituting the SIF range in one of the crack growth laws available from the literature [11], while Paris law [23] and the NASGRO equation [24] are used here. For describing the material behavior, both approaches resort to empirical fitting coefficients, which are taken directly from BS 7910:2013 or characterized at particular stress ratios. Crack length increment is obtained by

multiplying the crack growth rate by the number of cycles, and this increment is added to the previous crack length.

In step 3), the algorithm checks that the computed crack at the current iteration is acceptable under maximum load, using for that the Failure Assessment Diagram, as proposed by BS 7910:2013 [7]. This tool is applied for static assessments, and evaluates the acceptability of the flawed body in terms of brittle fracture and plastic collapse of the remaining ligament [25]. The last version of BS 7910 offers three *options* for generating the FAD curve that differentiates the safe and unsafe regions and for locating the evaluation point that describes the state of the flawed body [7].

From an industrial and practical point of view, there are several alternatives for applying the steps included in the methodology depicted in Figure 3. The degree of complexity and number of hypotheses vary from some alternatives to others, leading to predictions of distinct accuracy. In this work, three different alternatives are suggested for computing SIF range and for doing FAD evaluation, which are combined with two different ways of computing the crack growth rate. These alternatives are summarized in Table 1 and are explained below in greater detail. They are denoted Alternative 1, Alternative 2 and Alternative 3, being accompanied by a (G) or (C) whether generic (from literature) or characterized growth coefficients are used.

Table 1: Different alternatives for the methodology applied.

Alternative	**SIF calculation**	**Coefficients for** $\mathrm{d}a/\mathrm{d}N$	**FAD evaluation**
Alternative 1 (G)	$\Delta\sigma$ and ΔK analytically	Generic	Option 2 from
Alternative 1 (C)	(Figure 4a)	Characterized	BS 7910:2013
Alternative 2 (G)	$\Delta\sigma$ by FEA and ΔK	Generic	Option 2 from
Alternative 2 (C)	analytically (Figure 4b)	Characterized	BS 7910:2013
Alternative 3 (G)	ΔK by FEA	Generic	Option 3 from
Alternative 3 (C)	(Figure 4c)	Characterized	BS 7910:2013

2.1. SIF range calculation

2.1.1. Alternative 1: Analytical calculation of the SIF range based on remote stresses computed analytically

In Alternative 1, the SIF range is computed using the calibration of TC03 crack case from NASGRO manual [26] (Figure 4 a). This predefined geometry is similar to the one studied here, except for the fact that the crack must be located on the shortest one of the two ligaments, what does not happen in the present case. In order to overcome this problem, the components tested are assumed to be symmetric, with two equal ligaments at both sides of the hole. In this way, both ligaments are supposed to be as long as the shortest one in the real component and crack growth predictions are conservative.

TC03 crack case relates the stress intensity factor to remote stresses as shown in Figure 4a. In this particular study, only the membrane stress (S0, $\sigma_{\mathrm{m}}^{\mathrm{rem}}$) resulting from the applied axial force is considered, being calculated as the ratio between the magnitude of the force and the far-field cross-sectional area of the actual components. Note that e and H in equation (1) are thickness and width,

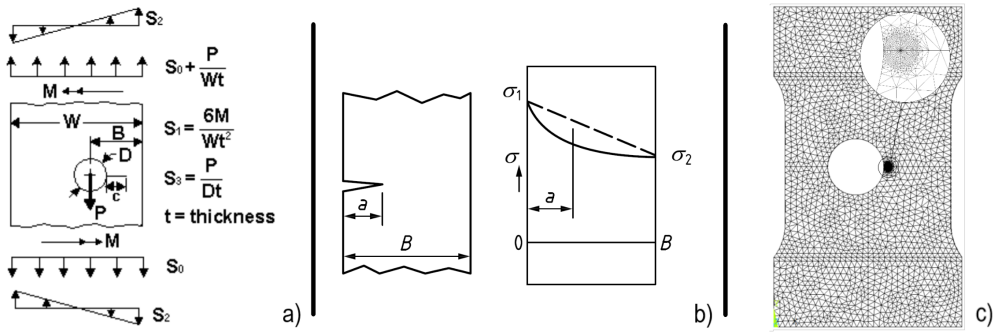

Figure 4: Notch and crack geometries for stress intensity factor calculation: a) through-crack from an offset hole in a plate [26], b) extended surface flaw in a plate [7] and c) finite element model of the cracked component.

respectively.

$$\Delta\sigma_{\mathrm{m}}^{\mathrm{rem}} = \frac{1}{eH}\Delta P \tag{1}$$

NASGRO software does not have closed-form formulas for the SIF calculation of built-in geometries, but rather interpolates between tabular data stored in its database. For a particular combination of remote membrane stress and crack length the relationship between stress and SIF, $\xi\,(a)$, is obtained in NASSIF module of NASGRO v8.1 software. Using expression (1), the SIF range in Alternative 1 is computed as (2).

$$\Delta K = \frac{\xi(a)}{eH}\Delta P \tag{2}$$

2.1.2. Alternative 2: Analytical calculation of the SIF range based on local stresses computed numerically

In Alternative 2, the formula applicable to extended surface flaws in plates (Figure 4b) is applied for SIF range computation (3). This crack growth case does not account for the fact that on the opposite side of the hole there is an uncracked ligament taking over part of the applied load.

$$\Delta K = \left(M_{\mathrm{m}}\Delta\sigma_{\mathrm{m}}^{\mathrm{loc}} + M_{\mathrm{b}}\Delta\sigma_{\mathrm{b}}^{\mathrm{loc}}\right)\sqrt{\pi a} \tag{3}$$

In equation (3) M_{m} and M_{b} are geometric factors defined in [7]. $\sigma_{\mathrm{m}}^{\mathrm{loc}}$ and $\sigma_{\mathrm{b}}^{\mathrm{loc}}$ are membrane and bending components of the local stresses calculated on the cracked ligament, omitting the presence of the flaw [7].

The local stress distribution may be calculated by finite element analysis. With this aim, an elastic model of the unflawed components is built in ANSYS v17.2, applying the pertinent boundary conditions (restricted displacements and rotations at both ends) and imposing the axial force. Then, the normal stress distribution is computed on the mid-plane of the longest ligament, where the stresses are slightly higher than at the free surfaces of the component. The irregular stress profile, which is higher at the hole edge due to stress concentration, is linearized so that the assumed stress is higher

than the actual one throughout the whole ligament (see Figure 4b). Membrane (4) and bending (5) stress components are obtained by [7]:

$$\sigma_{\mathrm{m}}^{\mathrm{loc}} = \frac{\sigma_1 + \sigma_2}{2} \tag{4}$$

$$\sigma_{\mathrm{b}}^{\mathrm{loc}} = \frac{\sigma_1 - \sigma_2}{2} \tag{5}$$

σ_1 and σ_2 are the maximum normal stress at the hole edge and the minimum normal stress at the end of the ligament, respectively (see Figure 4b). Based on the hypothesis of linear elastic material, both σ_1 and σ_2 are directly proportional to the load, that is, $\sigma_1 = \alpha P$ and $\sigma_2 = \beta P$. The proportionality constants α and β may be calculated under any load, and the membrane and bending components of local stress ranges may be expressed by (6) and (7).

$$\Delta\sigma_{\mathrm{m}}^{\mathrm{loc}} = \frac{\alpha + \beta}{2}\Delta P \tag{6}$$

$$\Delta\sigma_{\mathrm{b}}^{\mathrm{loc}} = \frac{\alpha - \beta}{2}\Delta P \tag{7}$$

Substituting equations (6) and (7) into (3), the SIF range is calculated as a function of the applied force range by:

$$\Delta K = \left(M_{\mathrm{m}}\left(\alpha + \beta\right) + M_{\mathrm{b}}\left(\alpha - \beta\right)\right)\frac{\Delta P}{2}\sqrt{\pi a} \tag{8}$$

2.1.3. Alternative 3: Calculation of the SIF range by FEA

In Alternative 3, the SIF range is obtained by finite element analysis. An elastic model of the flawed body is built in ANSYS v17.2 (Figure 4c). Young's modulus and Poisson's ratio of 42CrMo4 steel are assigned to the model. The bulk of the body is meshed using 10-node quadratic tetrahedrons with a nominal size three times smaller than the thickness dimension. In the crack region, 20-node quadratic hexahedrons are arranged following a radial/ring pattern (see Figure 4c), which are about 10 times smaller than the previous elements. Crack front is meshed using 15-node quadratic wedge elements. The model is fixed at the lower end by restricting displacements and rotation. The transversal movement and rotation are restricted at the upper end, and an axial force is applied on this zone. The stress intensity factor for a given combination of load and crack length is computed by means of contour integration.

2.1.4. Response curves for Alternatives 1, 2 and 3

Before starting the prediction algorithm, the crack case or finite element model is solved under a unitary force of 1 kN for several crack lengths ranging between the initial and final values, using NASGRO (Alternative 1) or ANSYS (Alternatives 2 and 3). Response curves, like the ones shown in Figure 5, are generated. Once the algorithm is operating, the unitary stress intensity factor for a particular crack length is interpolated from those curves. Subsequently, this value is multiplied by the load variation assuming linear elastic behavior of the material.

In Alternative 3 no simplifications are adopted regarding geometry so that loads and boundary conditions applied to the finite element model represent testing conditions faithfully. That is why the

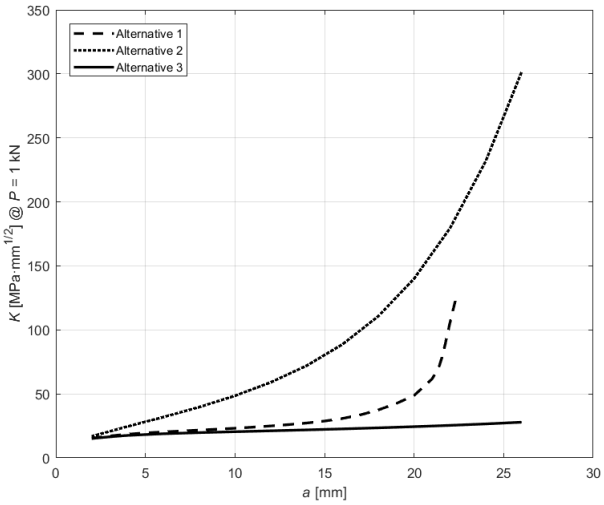

Figure 5: Response curve of the stress intensity factor for different crack lengths under an applied unitary force of 1 kN.

values belonging to this alternative are known to be the most realistic ones among the three response curves. In Alternative 1 the SIF is overestimated, with an error that increases with growing crack length. This is due to the assumption that there are two short ligaments at both hole sides (see section 2.1.1). For that reason, the estimated SIF grows asymptotically as the crack length reaches 22.5 mm, which is the length of the short ligament in this particular case (see Figure 8). The values from Alternative 2 are even more conservative, since the assumptions are focused on local stresses. This means that the stress distribution is computed numerically along the ligament where the prospective crack propagates, but avoiding the presence of the crack. Thereafter, as crack grows, Alternative 2 assumes that the initial net stress is redistributed entirely in the remaining ligament, omitting that on the opposite side of the hole there is an uncracked ligament. This explains why in Alternative 1, initially, the SIF is estimated correctly but for $a = 26$ mm it is overestimated by a factor of 10.

2.2. Crack increment computation and update of crack length

2.2.1. Alternative (G): Use of generic crack growth coefficients

In Alternative (G), generic coefficients are used in the crack growth rate calculation. In this case, these values are taken from the BS 7910:2013 [7] by considering the family of steels operating in air or other non-aggressive environments at temperatures up to 100 °C. This standard provides coefficients for Paris law (9), such as $C = 5.21\text{e}^{-13}$ and $n = 3$ for $\mathrm{d}a/\mathrm{d}N$ in mm/cycles and ΔK in MPamm$^{1/2}$.

$$\frac{\mathrm{d}a}{\mathrm{d}N} = C\Delta K^n \tag{9}$$

2.2.2. Alternative (C): Use of characterized crack growth coefficients

In Alternative (C), the crack growth law coefficients are obtained by fitting the NASGRO equation (10) to crack growth curves as characterized ad hoc for 42CrMo4 at different stress ratios. Contrary to Paris law, the NASGRO equation considers stress ratio and crack closure effects, and captures the

sigmoidal shape of crack growth curves in bi-logarithmic scale. The crack opening function, f, is calculated as in [27].

$$\frac{\mathrm{d}a}{\mathrm{d}N} = C\left[\frac{1-f}{1-R}\Delta K\right]^n \frac{\left(1-\frac{\Delta K_{\mathrm{th}}}{\Delta K}\right)^p}{\left(1-\frac{K_{\max}}{K_{\mathrm{c}}}\right)^q} \tag{10}$$

2.3. FAD evaluation

The BS 7910:2013 standard suggests the use of the Failure Assessment Diagram for predicting sudden failure of cracked components. Depending on the time and information available for the analysis, three different *options* can be applied to perform the evaluation. Here only Option 2 and Option 3 are implemented.

2.3.1. Alternative 1: Assessment line and evaluation point based on the Option 2 procedure

In Alternative 1, the Failure Assessment Diagram (FAD) is evaluated based on Option 2 procedure presented in BS 7910:2013 [7]. The assessment line that distinguishes the safe and unsafe regions is generated by the closed-form equation (11), where $\varepsilon_{\mathrm{ref}}$ is the true strain at the true stress $\sigma_{\mathrm{ref}} = L_{\mathrm{r}}\sigma_{\mathrm{y}}$. This implies the need for determining the characteristic coordinates of the $\sigma - \varepsilon$ tensile curve for the 42CrMo4 steel.

$$f\left(L_{\mathrm{r}}\right) = \left(\frac{E\varepsilon_{\mathrm{ref}}}{L_{\mathrm{r}}\sigma_{\mathrm{y}}} + \frac{L_{\mathrm{r}}^3\sigma_{\mathrm{y}}}{2E\varepsilon_{\mathrm{ref}}}\right)^{-1/2} \rightarrow 0 \leq L_{\mathrm{r}} < \frac{\sigma_{\mathrm{y}} + \sigma_{\mathrm{u}}}{2\sigma_{\mathrm{y}}} \tag{11}$$

The vertical coordinate of the evaluation point, K_{r}, is obtained as the ratio between the stress intensity factor for the crack length at the current iteration under maximum load and the fracture toughness. The horizontal coordinate, L_{r}, is computed as the ratio between the reference stress under maximum load and the yield strength of the material.

$$K_{\mathrm{r}} = \frac{K_{\max}}{K_{\mathrm{mat}}} \; ; \; L_{\mathrm{r}} = \frac{\sigma_{\mathrm{ref}}^{\max}}{\sigma_{\mathrm{y}}} \tag{12}$$

Since the predefined geometry selected in Alternative 1 (Figure 4a) is not contemplated by BS 7910:2013, no analytical formula can be applied for the reference stress calculation. Instead, the expression given in [26] is used for computing the maximum normal stress in the ligament.

2.3.2. Alternative 2: Assessment line and evaluation point based on the Option 2 procedure

In order to perform FAD evaluations, the assessment line for the Alternative 2 is the same one as that used in Alternative 1. The maximum stress intensity factor and the reference stress, as well as the corresponding ratios (K_{r} and L_{r}), are calculated analytically. The geometry for extended surface flaws (Figure 4b) is included for the calculation according to BS 7910:2013 so that all the required equations are taken from this standard.

2.3.3. Alternative 3: Assessment line and evaluation point based on the Option 3 procedure

In Alternative 3, the assessment line is derived using J-integral results from the elastic and elastic-plastic models of the component studied, by means of:

$$f\left(L_{\mathrm{r}}\right)=\sqrt{\frac{K}{K_J}} \tag{13}$$

The assessment line is forced to pass through a given K_{r} value at $L_{\mathrm{r}}=1$ [25], thus being independent of the crack length.

$$f\left(L_{\mathrm{r}}=1\right)=\left(1+\frac{0.002E}{\sigma_{\mathrm{y}}}+\frac{1}{2}\left(1+\frac{0.002E}{\sigma_{\mathrm{y}}}\right)^{-1}\right)^{-0.5} \tag{14}$$

The horizontal and vertical coordinates of the evaluation point are defined by:

$$K_{\mathrm{r}}=K_{\mathrm{r}}\left(P_{L_{\mathrm{r}}=1}\right)\frac{P_{\max}}{P_{L_{\mathrm{r}}=1}}\ ;\ L_{\mathrm{r}}=\frac{P_{\max}}{P_{L_{\mathrm{r}}=1}} \tag{15}$$

3. Simulation of crack growth using FRANC3D

Crack growth was simulated using the fracture analysis software FRANC3D 7.1.0 jointly with ANSYS v17.2 [28]. In this way, the different approaches consistent with the BS 7910:2013 standard are compared with state-of-the-art simulation tools that incorporate the latest research advances.

In FRANC3D, a sub-model of the crack propagation region was cropped from the global model of the components built previously in ANSYS. Then, an initial straight through-crack was created through the graphical user interface. The program remeshed the sub-model to insert the flaw, but the surface meshes of the faces shared by sub-model and global model were not modified (see Figure 6). Externally, the cracked portion and the global model were combined, and the stress analysis was executed in ANSYS. Thereafter, the results were read in FRANC3D, and the stress intensity factors along the crack front were calculated by the M-integral approach [29].

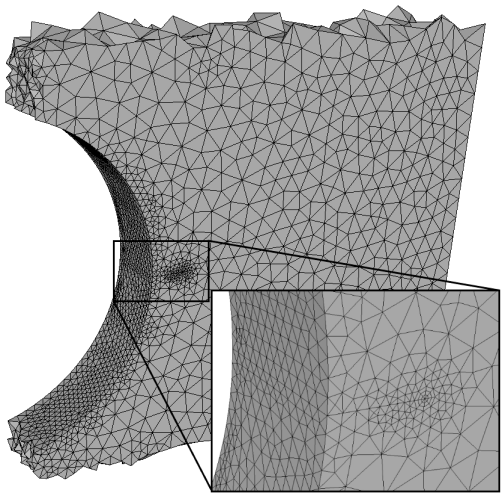

Figure 6: Mesh of the sub-model representing the crack growth region of the components. A close-up of the initial crack ($a=3$ mm) is shown.

The crack extension at any point i in the crack front was computed as a function of a user-prescribed median crack extension (Δa_{med}):

$$\Delta a_i = \Delta a_{\text{med}} \left(\frac{K_i}{K_{\text{med}}} \right)^2 \tag{16}$$

The new crack fronts generated by connecting different points exhibited a piecewise linear shape that could be smoothed using a third order polynomial spline [16]. These steps were executed iteratively for several successive steps.

The loading schedule was defined as a simple cyclic profile where K varied indefinitely between maximum and minimum values applied during the tests. The main output of FRANC3D was the crack length at any point of the crack front as a function of the elapsed cycles.

4. Material characterization and fatigue testing of components

4.1. Material characterization

42CrMo4 steel is very often used in bearing rings for wind turbine blades because its excellent hardenability properties that permit to achieve high hardness on the raceway of the rollers [3]. In this work, the properties of this steel were characterized, which are needed for applying the methodology presented in section 2.

Validation components, Compact Tension (CT) specimens for crack growth curve characterization and cylindrical specimens for determination of tensile properties were extracted from a real wind turbine bearing ring subjected to bulk tempering (see Figure 7). Validation components and CT specimens were oriented so that the crack would grow in the radial direction, as observed at rings in operation (see Figure 1b).

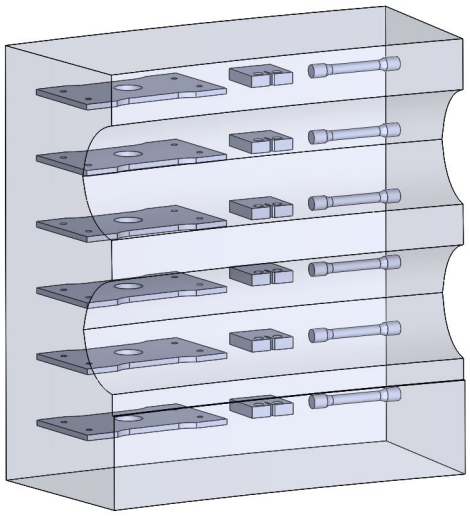

Figure 7: Position and orientation of validation components and characterization specimens inside the bearing ring.

The tensile properties such as yield strength, ultimate tensile strength and Young's modulus were determined according to UNE-EN ISO 6892-1:2010. Crack growth curves were obtained according to

ASTM E647-15 standard at the stress ratios of interest. Those curves were fitted independently using the NASGRO equation (10) in NASMAT module of NASGRO v8.1 software allowing the C, n, p and q fitting coefficients for the NASGRO equation to be found.

4.2. Geometry of validation components

The validation components consisted in 6 mm thick plates with a 60 mm long calibrated central region presenting a hole drilled asymmetrically (Figure 8). In the 35.5 mm long ligament, a 2 mm long and approximately 0.25 mm wide precrack was performed by wire electric discharge machining (Detail C). In the upper and lower ends knurled blocks were attached to the testing fixture for gripping.

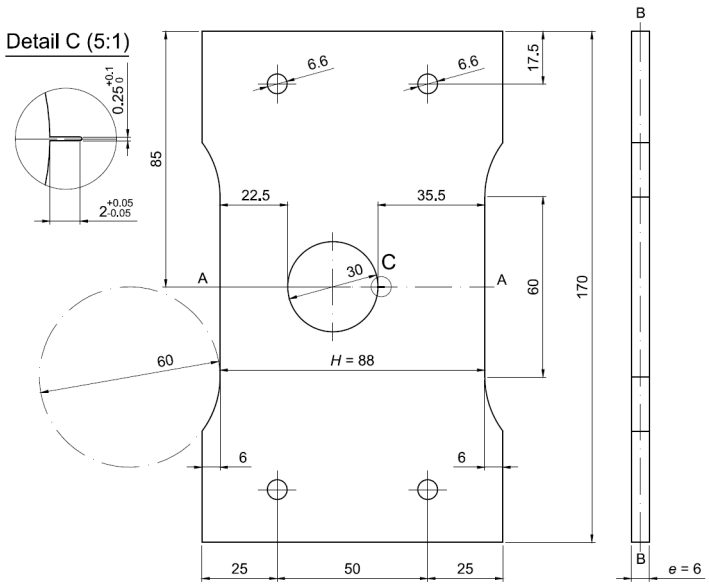

Figure 8: Geometry of the tested components. Dimensions in millimeters.

4.3. Testing conditions for validation components

The components were tested under load control, by applying a sinusoidal axial force at a frequency of 15 Hz. In all the tests, the maximum force value was confined to 50 kN, which corresponded to a remote stress ($\sigma^{\text{rem}} = P/(eH)$) of 94.70 MPa (see Table 2), so that linear behavior of the material prevailed at the crack tip throughout the propagation and small scale yielding could be assumed.

Tests were carried out at three different stress ratios, namely $R = 0.1$, 0.35 and 0.6, whereby each test was repeated twice using two different specimens. The values for the stress ratios were chosen according to the rainflow matrix assessed for a real wind turbine bearing ring.

Table 2: Maximum values and ranges of applied forces and stresses.

Test	**Spec. ID**	R [-]	$P_{\max}$; ΔP **[kN]**	$\sigma^{\text{rem}}_{\max}$; $\Delta\sigma^{\text{rem}}$ **[MPa]**	$\sigma^{\text{net}}_{\max}$; $\Delta\sigma^{\text{net}}$ **[MPa]** ($a = 3$ mm)	$\sigma^{\text{net}}_{\max}$; $\Delta\sigma^{\text{net}}$ **[MPa]** ($a = 25.5$ mm)
1	OH_P1 & OH_P2	0.1	50 ; 45	94.70 ; 85.23	151.5 ; 136.4	256.4 ; 230.8
2	OH_P5 & OH_P6	0.35	50 ; 32.5	94.70 ; 61.55	151.5 ; 98.48	256.4 ; 166.67
3	OH_P3 & OH_P4	0.6	50 ; 20	94.70 ; 37.88	151.5 ; 60.61	256.4 ; 102.6

A SERVOSIS MUF-401/15 hydraulic testing machine with a maximum load capacity of 150 kN, equipped with a HBM U5 force transducer, was used in the experimental campaign (Figure 9, left).

Crack length was measured on both faces of the components using crack detection gauges (Figure 9, right), from 3 mm up to 22.5 mm or 25.5 mm, depending on the crack gauge. The maximum net section stress ($\sigma_{\max}^{\text{net}} = P/e/(H-a)$) varied from 151.5 MPa to 265.4 MPa, as shown in Table 2.

The previous growth from the end of the 2 mm-long starter notch to 3 mm was excluded from the analysis with the aim of eliminating blunt tip effects [30]. In order to validate the gauge measurements, the tests were interrupted at certain times, and components were dismounted from the fatigue machine to observe them in a Nikon SMZ645 microscope. Both measuring techniques provided very similar values. Crack length at the end of stable crack growth was measured visually by post-mortem inspection of the fracture surfaces.

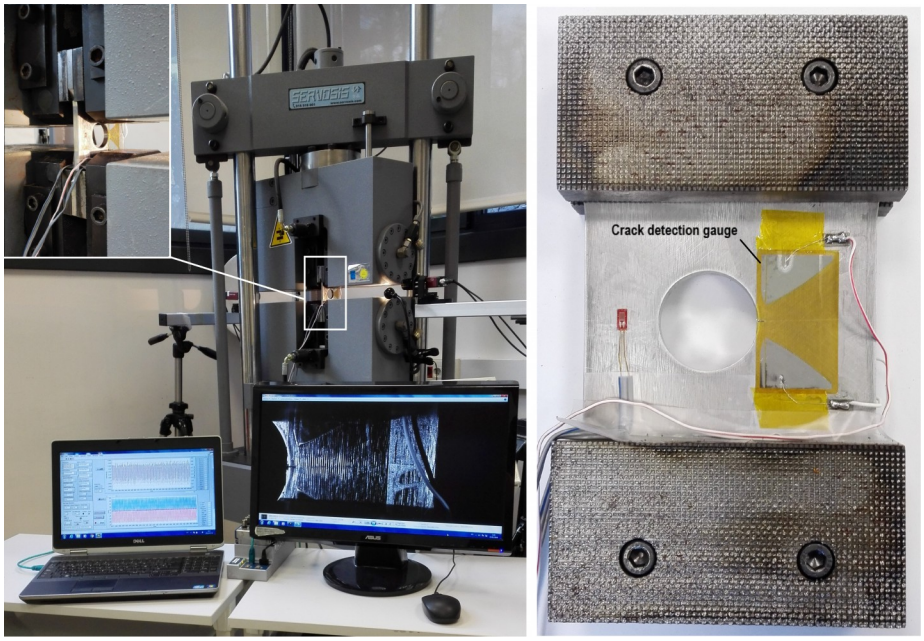

Figure 9: Photographs of the testing setup (left) and a component (right).

5. Results and discussion

5.1. Experimental results at different stress ratios and force ranges

Figure 10 shows the experimental evolution of the crack length with respect to the number of cycles under three different testing conditions (see Table 2).

The results from the components tested at identical conditions show high repeatability, with relative differences below 15% in number of cycles throughout great part of the measured crack growth extent. The last points of each curve indicate the onset of unstable propagation, where sudden failure of the remaining ligament occurs.

While keeping the maximum applied force constant at 50 kN, average fatigue life increases with decreasing force range and increasing stress ratio. For $\Delta P = 45$ kN and $R = 0.1$ the fatigue life

extends over 200 kcycles, for $\Delta P = 32.5$ kN and $R = 0.35$ the lifetime increases up to 500 kcycles, approximately, and for $\Delta P = 20$ kN and $R = 0.6$ the components are able to sustain around 1700 kcycles before catastrophic failure occurs. The six components fail suddenly at $a = 33.5 - 34$ mm when the remaining ligament is about $1.5 - 2$ mm long, regardless of testing conditions.

Increasing force range and stress ratio are known to have opposite effects on the crack growth rate [31], but in this particular case the change in the magnitude of the former is predominant. In addition, the fact that collapse occurs always at same critical crack length indicates that the final failure is governed, as expected, by the maximum stress intensity factor [16] resulting from the maximum force, which is kept constant in all the tests.

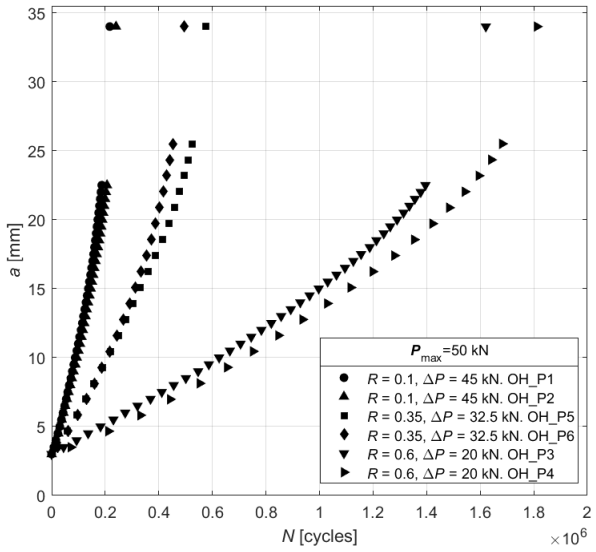

Figure 10: Experimental crack growth in function of cycles measured for different testing conditions.

5.2. Comparison between BS 7910:2013 predictions and experimental results

Figure 11 shows the BS 7910:2013 predictions and experimental results of the crack length as a function of time. Each graph corresponds to a given set of testing conditions from Table 2 and predictions are done according to alternatives summarized in Table 1.

5.2.1. Alternatives 1 (G), 1 (C), 2 (G) and 2 (C)

For all cases, Alternatives 1 and 2 overestimate the crack propagation rate significantly and predict catastrophic collapse prematurely in terms of the number of cycles to failure. Alternative 2 (G) is the most conservative prediction in the three scenarios, underestimating fatigue life by more than 96%. Among Alternatives 1(G), 1(C), 2 (G) and 2 (C), Alternative 1 (C) is the one yielding the closest results to the experimental values, though the error in number of cycles to failure is around or over 50% depending on testing conditions. There are no clear differences between Alternatives 1 (G) and 2 (C). They provide similar results for the first two load cases, with errors up to 87-88% in the number of cycles, but the former is better for the last scenario (errors of 82.6% and 90.4%, respectively). These relative differences are referred to mean experimental values.

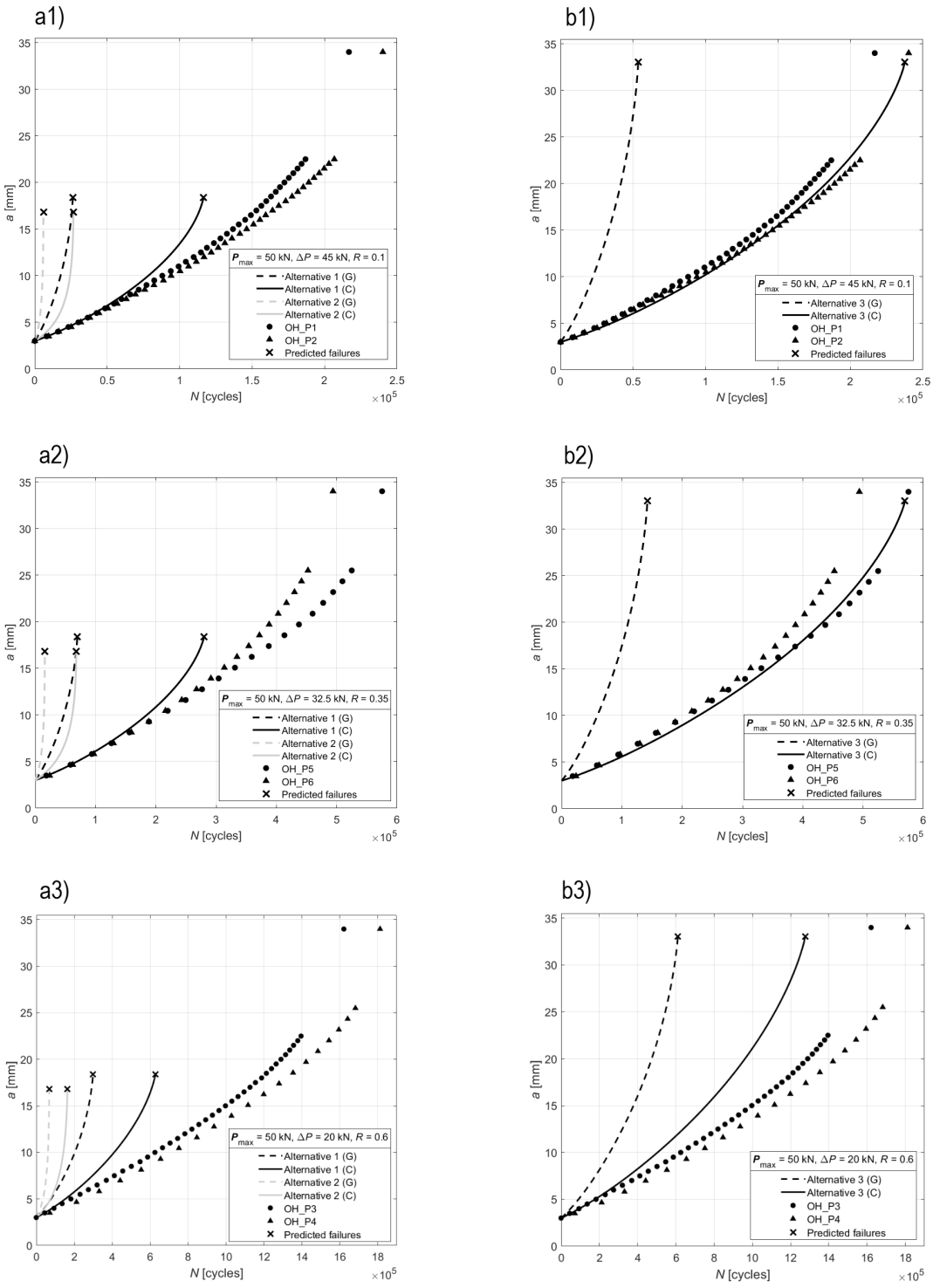

Figure 11: Experimental and predicted crack growth as a function of cycles under different testing conditions. a) Alternative 1 and 2 predictions. b) Alternative 3 predictions.

Alternatives 1 and 2 estimate the critical crack lengths of 18.38 mm and 16.82 mm, respectively. These values are about half of the experimental ones, with errors of 45.9% and 50.5%. Predicted critical crack length depends neither on R ratio and force range nor on the fatigue growth properties, which is consistent with experimental observations.

As expected, the use of crack growth curves characterizing the material at the particular stress ratio helps to enhance predictions significantly, particularly in Alternative 1. However, the error made in calculating the stress intensity factor renders the predictions of fatigue failure too conservative for both Alternatives 1 and 2.

The results show that Alternatives 1 and 2 are valid for preliminary and conservative estimations though none of them is suitable for acceptable prediction of crack propagation. The discrepancies among Alternatives 1, 2 and 3 in the estimation of crack length as a function of time are determined exclusively by the large differences shown by the computed stress intensity factors (Figure 5). Discrepancies in failure detection are also caused predominantly by SIF variations, because the assessment line used in failure evaluation is almost identical in all the alternatives.

The predictions from Alternative 2 are less accurate than those from Alternative 1, what means that it is not worth building a finite element model for the uncracked body for computing local stresses. Such a study is time-consuming that does not contribute to improve predictions.

5.2.2. Alternatives 3 (G) and 3 (C)

Alternative 3 (G) is very conservative to estimate the lifetime to collapse, leading to errors around (65-75%). However, that alternative predicts the final crack length accurately (33.05 mm *vs.* $\approx$ 34 mm), with an error below 3% for any case. Alternative 3 (C) is as good as Alternative 3 (G) for estimating critical crack length, also improving remarkably the estimation of the number of cycles to failure. In the first two testing conditions, fatigue lives predicted by Alternative 3 (C) are only 3.94% and 6.54% higher than the experimental average lives, whereas in the last case ($R = 0.6$) the expected life is shorter by 25.6%.

Again, the characterization of crack growth curve is crucial allowing excellent predictions of a vs. N at $R = 0.1$ and $R = 0.35$ to be obtained. The prognosis deviates considerably from the experimental measurements at $R = 0.6$, what could be assigned to the fact that the NASGRO equation, used here for describing crack growth, suppresses crack closure at $R = 0.6$.

It follows that Alternative 3 (G) is not recommended for predicting crack length in time accurately, which is essential for programming an inspection plan, for instance. However, that alternative is ideal for determining the critical crack length, which represents a failure criterion. If an accurate calculation of the crack length evolution is needed, the stress intensity factor has to be calculated for the exact geometry of the cracked component, and material crack growth curve has to be characterized at the stress ratio of interest, as in Alternative 3 (C). However, small calculation errors may lead to slightly different predictions falling on the unsafe side.

5.3. Comparison among Alternative 3 (C) predictions, FRANC3D simulations and experimental results

Figure 12 shows the experimental mean values of the crack length at the component face and the results of simulations performed in FRANC3D under different testing conditions using characterized crack growth properties. The predictions of the most accurate BS 7910:2013 methodology are included.

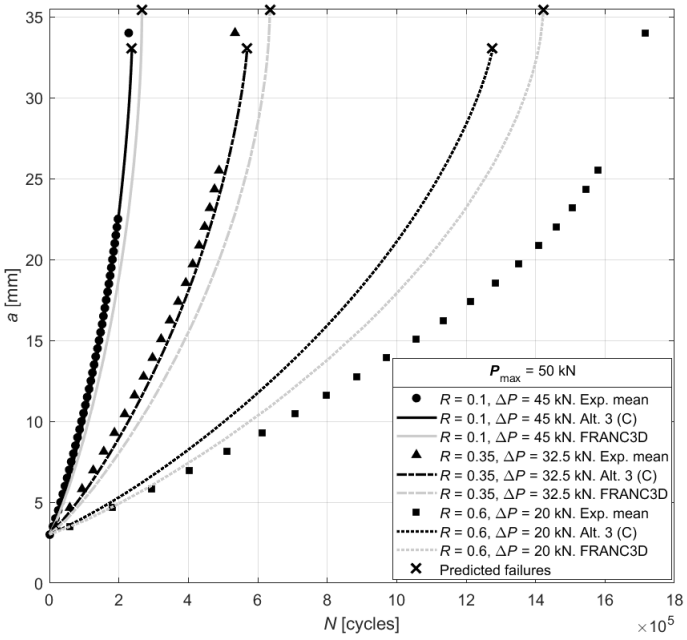

Figure 12: Evolution of the crack length at component face: experimental mean values and predictions according to FRANC3D and Alternative 3 (C).

At $R = 0.1$ and $R = 0.35$, the results of the simulations performed using FRANC3D are non-conservative in terms of the critical length of crack and the number of cycles to failure. In both scenarios, the expected life according to this program is about 17-19% longer than that measured, and in any case, the complete failure of the components is predicted when there is no uncracked ligament left ($a \approx 35.5$ mm). This means that the critical crack length is overestimated by 5%, approximately.

At $R = 0.6$, FRANC3D underestimates fatigue life by 17% with respect to experimental mean. As opposed to the results at other testing conditions, the predicted crack length is higher than the real one for any time. However, the critical crack length does not change among simulations, because it is given by the maximum load, and it is 5% higher than measured, also at $R = 0.6$.

The overestimation of the critical crack length in FRANC3D can be assigned to the fact that the Failure Assessment Diagram evaluation is not implemented, whereas only the condition $K_{\max} < K_{\mathrm{mat}}$ is verified, as considered by the vast majority of authors [16, 32, 33].

For the three loading cases, FRANC3D underestimates the crack growth compared to Alternative 3 (C). Since NASGRO equation provided with the fitted coefficients is used in both cases, the differences can be attributed exclusively to the different way of calculating the stress intensity factor. FRANC3D results are supposed to be more reliable than those of Alternative 3 (C), because no assumptions are made regarding magnitude and direction of the crack advance. In Alternative 3 (C), the crack front is forced to be straight, and the advance is driven by the maximum value of SIF at the midpoint of the crack front. This premise of FRANC3D being more accurate than Alternative 3 (C) is not fulfilled at the first two scenarios.

Figure 13 shows the crack evolution for any load range and stress ratio, simulated using FRANC3D combined with ANSYS. A median crack advance of 1 mm was chosen up to a length of 30 mm, while from that point on the advance was reduced to facilitate remeshing and convergence of the stress analysis.

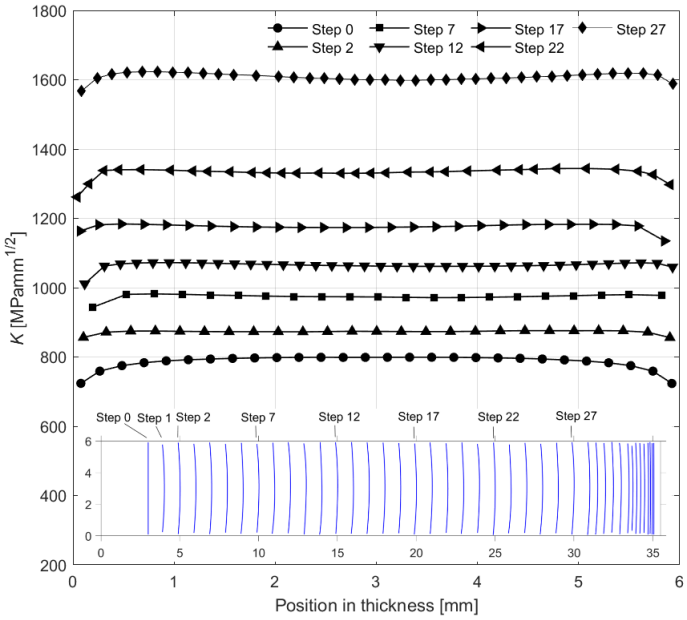

Figure 13: Simulated crack fronts and stress intensity factor profiles for certain steps.

The crack starts as a straight line, then bends and eventually returns to the original straight shape. This transition of the crack front shape is caused by the distribution of the stress intensity factor range along the crack front and its variation as crack advances. At the initial crack front (Step 0) the stress intensity factor is maximum at the mid-thickness, which propitiates larger crack growth at the central region than at the edges, which is known as crack tunnelling phenomenon [25]. As a result, the arc-shaped configuration is observed at Step 1 shown in Figure 13.

During the following successive steps shown in Figure 13 (Steps 2-7-12-17-22), the stress intensity factor remains relatively constant throughout the thickness with sudden decreases at the edges, while the curved cracked front advances uniformly. From Step 27 onward, the stress intensity factor profile has a valley at the mid-thickness. At the final propagation phase, the points located at the outer region propagate faster so that the crack fronts almost recover the straight profile again.

6. Conclusions

In this work the growth of a hole-edge crack propagating in 42CrMo4 steel under mode-I cyclic loading was predicted analytically, simulated and measured experimentally. Analytical predictions were performed based on the BS 7910:2013, resorting to different alternatives of increasing complexity. On the other hand, crack growth for that particular geometry, material and loading was simulated

jointly in FRANC3D and ANSYS. A quantitative and critical comparison with experimental results led to the following conclusions.

Regarding the estimation of critical crack length:

- Contrary to any logical expectation, a more sophisticated calculation of the stress intensity factor may not contribute to enhancing the estimation of the critical crack length. The numerical calculation of the local stresses in the uncracked body does not necessarily improve the prediction of the critical crack length performed following purely analytical alternatives that compute both stress and stress intensity factor using closed-form expressions. In this case, the former was less accurate, yielding a critical crack length 50% lower than that measured experimentally.

- The optimal way to obtain a reasonable estimation of the critical crack length implies calculating the stress intensity factor for the exact cracked component geometry using finite element methods. For ductile fracture, the Failure Assessment Diagram (FAD) should be used as a failure criterion, because brittle fracture criterion ($K_{\max} < K_{\mathrm{mat}}$) yields non-conservative results. In this case, the FAD-based predictions provided a critical crack length 3% lower than experimental ones, whereas this variable was overestimated by 5% considering brittle fracture exclusively.

Regarding the estimation of number of cycles to failure:

- Once again, it may not be advisable to compute local stresses numerically, since the predicted number of cycles to failure may be less reliable than that obtained using analytical expressions. In this case, using a generic crack growth law, the total fatigue life was underestimated by more than 96% for any load range or stress ratio.

- For obtaining acceptable predictions, it is indispensable to use 1) numerically calibrated stress intensity factors and 2) crack growth coefficients fitted to growth curves measured at corresponding stress ratios. In this case, this allowed the estimation of fatigue lives with errors of 3.96% and 6.51% at stress ratios of 0.1 and 0.35. At $R = 0.6$ predictions were less reliable, with errors around 26% on the safe side.

- In this case, simulating crack growth by iterative remeshing changed the previously mentioned predictions slightly, due to minor variations in stress intensity factors. However, differences should be evaluated in the real complex geometry of the cracked wind turbine bearing.

Acknowledgements

The authors would like to thank Laulagun Bearings for sharing their broad know-how in wind turbine bearings and for providing the 42CrMo4 steel block from which specimens were manufactured.

References

[1] R. Budny, Improving pitch bearing reliability (2016).
URL http://www.rbbengineering.com/wp-content/uploads/2016/03/RBB-Pitch-Bearing-Reliability-Presentation.pdf

[2] LIEBHERR.
URL https://www.liebherr.com/en/deu/products/wind-energy/wind-energy.html{#}!/content=cp-wind-energy-tab-components

[3] P. Göncza, R. Potočnik, S. Glodež, Fatigue behaviour of 42CrMo4 steel under contact loading, Procedia Engineering 2 (1) (2010) 1991–1999. doi:10.1016/J.PROENG.2010.03.214.

[4] J. B. Wintle, Which procedures for fitness-for-service assessment: API 579 or BS 7910?, Proceedings of the International Conference on Pressure Vessel Technology, ICPVT.

[5] N. Larrosa, R. Ainsworth, Comparisons of the Solutions of Common FFS Standard Procedures to Benchmark Problems, Procedia Engineering 130 (2015) 1327–1342. doi:10.1016/j.proeng.2015.12.303.

[6] N. Larrosa, R. Ainsworth, R. Akid, P. Budden, C. Davies, I. Hadley, D. Tice, A. Turnbull, S. Zhou, 'Mind the gap' in fitness-for-service assessment procedures-review and summary of a recent workshop, International Journal of Pressure Vessels and Piping 158 (2017) 1–19. doi:10.1016/J.IJPVP.2017.09.004.

[7] Guide to methods for assessing the acceptability of flaws in metallic structures, 3rd Edition, British Standards Institution, 2013.

[8] G. Lesiuk, P. Kucharski, J. A. Correia, A. D. Jesus, C. Rebelo, L. S. da Silva, Mixed mode (i+ii) fatigue crack growth in puddle iron, Engineering Fracture Mechanics 185 (Supplement C) (2017) 175 – 192, xVIII International Colloquium Mechanical Fatigue of Metals. doi:https://doi.org/10.1016/j.engfracmech.2017.05.002.

[9] J. A. Correia, A. M. De Jesus, A. L. Silva, B. Pedrosa, C. Rebelo, R. A. Calçada, FE simulation of S-N curves for a riveted connection using two-stage fatigue models, Advances in Computational Design 2 (2017) 333–349. doi:10.12989/acd.2017.2.4.333.

[10] P. G. Nittur, A. M. Karlsson, L. A. Carlsson, Numerical evaluation of Paris-regime crack growth rate based on plastically dissipated energy, Engineering Fracture Mechanics 124-125 (2014) 155–166. doi:10.1016/J.ENGFRACMECH.2014.04.013.

[11] G. Lesiuk, M. Szata, D. Rozumek, Z. Marciniak, J. Correia, A. De Jesus, Energy description of fatigue crack growth process - theoretical and experimental approach, Procedia Structural Integrity 5 (2017) 904–911. doi:10.1016/J.PROSTR.2017.07.128.

[12] S. Razavi, M. Ayatollahi, C. Sommitsch, C. Moser, Retardation of fatigue crack growth in high strength steel s690 using a modified stop-hole technique, Engineering Fracture Mechanics 169 (Supplement C) (2017) 226 – 237. doi:https://doi.org/10.1016/j.engfracmech.2016.11.013.

[13] H. Richard, M. Sander, B. Schramm, G. Kullmer, M. Wirxel, Fatigue crack growth in real structures, International Journal of Fatigue 50 (2013) 83–88. doi:10.1016/J.IJFATIGUE.2012.02.013.

[14] D. F. Peixoto, P. M. de Castro, Fatigue crack growth of a railway wheel, Engineering Failure Analysis 82 (2017) 420–434. doi:10.1016/J.ENGFAILANAL.2017.07.036.

[15] Q.-Q. Yu, Y.-F. Wu, Fatigue durability of cracked steel beams retrofitted with high-strength materials, Construction and Building Materials 155 (2017) 1188–1197. doi:10.1016/J.CONBUILDMAT.2017.09.051.

[16] X. Zhang, L. Li, X. Qi, J. Zheng, X. Zhang, B. Chen, J. Feng, S. Duan, Experimental and numerical investigation of fatigue crack growth in the cracked gear tooth, Fatigue & Fracture of Engineering Materials & Structures 40 (7) (2017) 1037–1047. doi:10.1111/ffe.12557.

[17] M. Ayatollahi, S. Razavi, H. Chamani, Fatigue life extension by crack repair using stop-hole technique under pure mode-i and pure mode-ii loading conditions, Procedia Engineering 74 (2014) 18 – 21, xVII International Colloquium on Mechanical Fatigue of Metals (ICMFM17). doi:https://doi.org/10.1016/j.proeng.2014.06.216.

[18] C. H. R. Ayatollahi M R, Razavi S M J, A numerical study on the effect of symmetric crack flank holes on fatigue life extension of a sent specimen, Fatigue & Fracture of Engineering Materials & Structures 37 (10) 1153–1164. doi:10.1111/ffe.12199.

[19] M. R. Ayatollahi, S. M. J. Razavi, M. Y. Yahya, Mixed mode fatigue crack initiation and growth in a ct specimen repaired by stop hole technique, Engineering Fracture Mechanics 145 (2015) 115 – 127. doi:https://doi.org/10.1016/j.engfracmech.2015.03.027.

[20] M. R. Ayatollahi, S. M. J. Razavi, C. Sommitsch, C. Moser, Fatigue life extension by crack repair using double stop-hole technique, in: THERMEC 2016, Vol. 879 of Materials Science Forum, Trans Tech Publications, 2017, pp. 3–8. doi:10.4028/www.scientific.net/MSF.879.3.

[21] H. Liu, X.-L. Zhao, R. Al-Mahaidi, Boundary element analysis of cfrp reinforced steel plates, Composite Structures 91 (1) (2009) 74 – 83. doi:https://doi.org/10.1016/j.compstruct.2009.04.032.

[22] Q. Yu, X. Zhao, T. Chen, X. Gu, Z. Xiao, Crack propagation prediction of cfrp retrofitted steel plates with different degrees of damage using bem, Thin-Walled Structures 82 (2014) 145 – 158. doi:https://doi.org/10.1016/j.tws.2014.04.006.
URL http://www.sciencedirect.com/science/article/pii/S0263823114001190

[23] P. Paris, F. Erdogan, A Critical Analysis of Crack Propagation Laws, Journal of Basic Engineering 4 (1963) 528–834. doi:10.1115/1.3656900.

[24] R. Forman, S. Mettu, Behavior of Surface and Corner Cracks Subjected to Tensile and Bending Loads in Ti-6Al-4V Alloy, Tech. rep., NASA (1990).

[25] T. Anderson, Fracture Mechanics: Fundamentals and Applications, 3rd Edition, CRC Press, Boca Raton, 2005.

[26] NASA, NASGRO. Reference manual (2016).

[27] J. J. Newman, A crack opening stress equation for fatigue crack growth, International Journal of fracture 24 (4) (1984) R131–R135.

[28] Y. Yang, M. Vormwald, Fatigue crack growth simulation under cyclic non-proportional mixed mode loading, International Journal of Fatigue 102 (2017) 37–47. doi:10.1016/J.IJFATIGUE.2017.04.014.

[29] J.-H. Kim, G. H. Paulino, Consistent formulations of the interaction integral method for fracture of functionally graded materials, Journal of Applied Mechanics 72 (3) (2005) 351–364. doi:10.1115/1.1876395.

[30] Standard Test Method for Measurement of Fatigue Crack Growth Rates, ASTM International, 2015. doi:10.1520/E0647-15.

[31] R. Seifi, R. Hosseini, Experimental study of fatigue crack growth in raw and annealed pure copper with considering cyclic plastic effects, Theoretical and Applied Fracture Mechanics 94 (2018) 1–9. doi:10.1016/J.TAFMEC.2017.12.003.

[32] B. Davis, P. Wawrzynek, A. Ingraffea, 3-D simulation of arbitrary crack growth using an energy-based formulation – Part I: Planar growth, Engineering Fracture Mechanics 115 (2014) 204–220. doi:10.1016/J.ENGFRACMECH.2013.11.005.

[33] B. Davis, P. Wawrzynek, B. Carter, A. Ingraffea, 3-D simulation of arbitrary crack growth using an energy-based formulation – Part II: Non-planar growth, Engineering Fracture Mechanics 154 (2016) 111–127. doi:10.1016/J.ENGFRACMECH.2015.12.033.